Supporting Information

Electrical and UV-Sensing Performance of N-doped-Ba(Ti,Zr,Mo,Hf,Ta)O_3-Dielectric and ZnSnO-Channel-Based Flexible Thin-Film Transistors

Van Dung Nguyen[1], Takahiro Nagata[2], Huu Duc Luong[3], and K.-S. Chang[1,]*

[1] Department of Materials Science & Engineering, National Cheng Kung University.

No.1, University Road, Tainan City 70101, Taiwan.

[2] Research Center for Electronic and Optical Materials, National Institute for Materials Science.

1-1 Namiki, Tsukuba, Ibaraki 305-0044, JAPAN.

[3]Laboratory for Chemistry and Life Science (CLS), Institute of Innovative Research (IIR), Tokyo Institute of Technology.

R1-25, 4259 Nagatsuta-cho, Midori-ku, Yokohama, 226-8501, JAPAN.

[*]e-mail: kschang@mail.ncku.edu.tw; Tel.: +886-6-2757575 ext. 62922.

Figure S1

The constituent elements (at.%) across the N-doped Ba(Ti,Zr,Mo,Hf,Ta)O_3 film library were quantitatively determined using scanning XRF, and the results are displayed in **Figure S1**. Oxygen and nitrogen are excluded because of their weak fluorescence signals. Three-dimensional (3D) surface mapping for each element was performed to elucidate their distributions. The Ba (Figure S1a) and Ti (Figure S1b) variations) decrease similarly, as indicated by the dashed arrow in the figures. There are also consistent decreasing trends for Hf (Figure S1c) and Ta (Figure S1d), and Zr (Figure S1e) and Mo (Figure S1f), as indicated by the dashed arrows. The observed elemental distributions are in accordance with our experimental design.

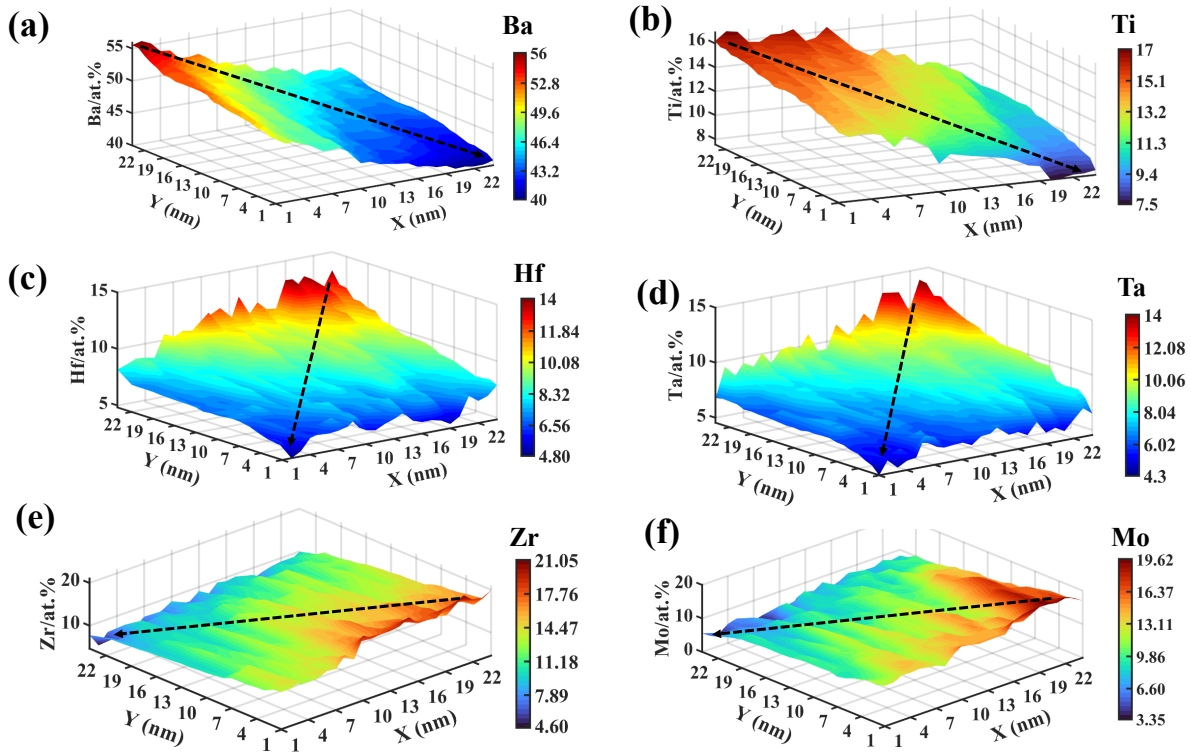


Figure S1. Scanning XRF results of the N-doped Ba(Ti,Zr,Mo,Hf,Ta)O_3 film library.

Figure S2

XPS of Ba(Ti,Zr,Mo,Hf,Ta)O_3 with and without N doping were studied. The peaks of constitutive elements on the B site shift to higher binding energy after N doping (upper spectra, **Figure S2**) compared with those without N doping (lower spectra, **Figure S2**), which was resulted from the difference in electron density (lower electronegativity of N than O). The V_O concentration reduces from ≈25.7 to 13.97 at.% after N doping, indicating a decrease in the defect of the dielectric layer. This is consistent with our results in the bias stress study (**Figures 9–11**).

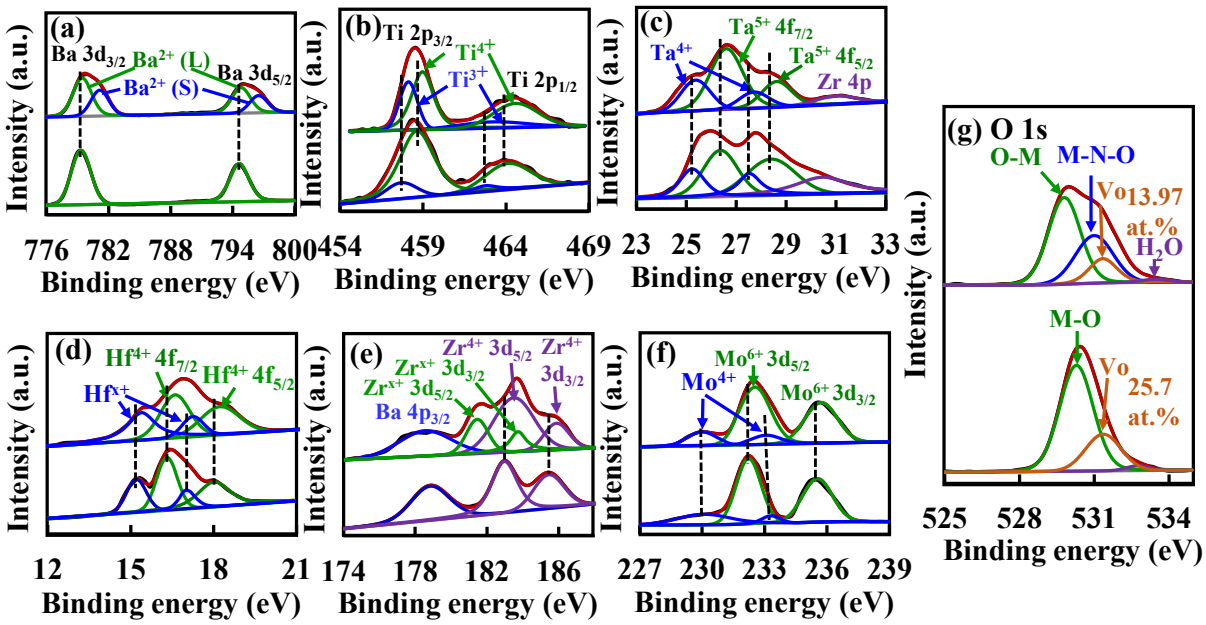


Figure S2. XPS results of N-doped Ba(Ti,Zr,Mo,Hf,Ta)O_3 (upper spectra in all figures) and Ba(Ti,Zr,Mo,Hf,Ta)O_3 (lower spectra in all figures): (a) Ba 3d, (b) Ti 2p, (c) Ta 4f, (d) Hf 4f, (e) Zr 3d, and (f) Mo 3d and (g) O 1s.

Figure S3

The high-resolution XPS results of ZnSnO are displayed in **Figure S3**. The Zn 2p spectrum (**Figure S3a**) exhibits two distinct peaks at approximately 1021.7 and 1044.9 eV, ascribed to Zn^{2+} $2p_{3/2}$ and Zn^{2+} $2p_{1/2}$, respectively [S1]. In the Sn 3d spectrum (**Figure S3b**), two peaks at 486.05 and 494.52 eV are associated with Sn^{4+} $3d_{5/2}$ and Sn^{4+} $3d_{3/2}$, respectively [S1]. The O 1s spectrum (**Figure S3c**) reveals three deconvoluted subpeaks: lattice oxygen (O_L) at approximately 530.51 eV, V_O (≈9.67 at.%.) at approximately 531.8 eV, and H_2O at approximately 532.4 eV [S1].

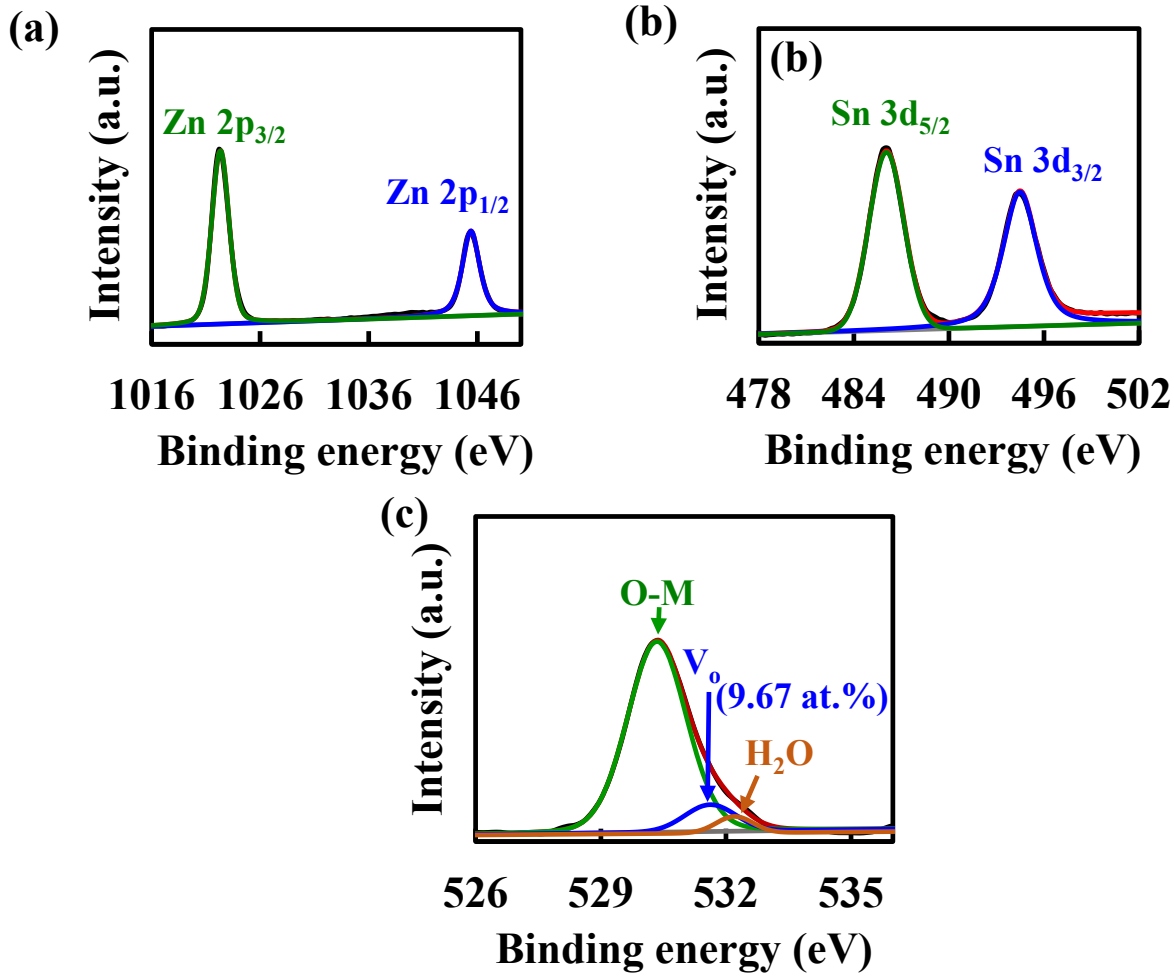


Figure S3. High-resolution XPS spectra of ZnSnO: (a) Zn 2p, (b) Sn 3d, and (c) O 1s.

[S1] Q. Zhang, C. Ruan, H. Gong, G. Xia, S. Wang, Low-temperature and high-performance ZnSnO thin film transistor activated by lightwave irradiation, Ceram. Int. 47 (2021) 20413-20421. https://doi.org/10.1016/j.ceramint.2021.04.050.

Figure S4

Figure S4a shows four PL emission bands (≈360, 409.1, 550, and 705 nm) of N-doped Ba(Ti,Zr,Mo,Hf,Ta)O_3. The emission at 409.1 nm is due to shallow defects (*e.g.*, V_O). The emission at 550 nm is associated with the recombination of induced electron–hole pairs due to the surface state. The emission at 705 nm is ascribed to the presence of defects such as Ti^{3+} interstitials or Ti^{3+} vacancies. **Figure S4b** shows the PL spectrum of ZnSnO. The strong luminescence band at ≈335 nm is due to the recombination of free excitons in an energy level close to the band edges of ZnSnO. The emissions at 412 and 545 nm are ascribed to electron transitions from the shallow and deep Vo levels to E_C, respectively. The emission at 700 nm is associated with the presence of defects such as Zn vacancies and/or oxygen interstitials.

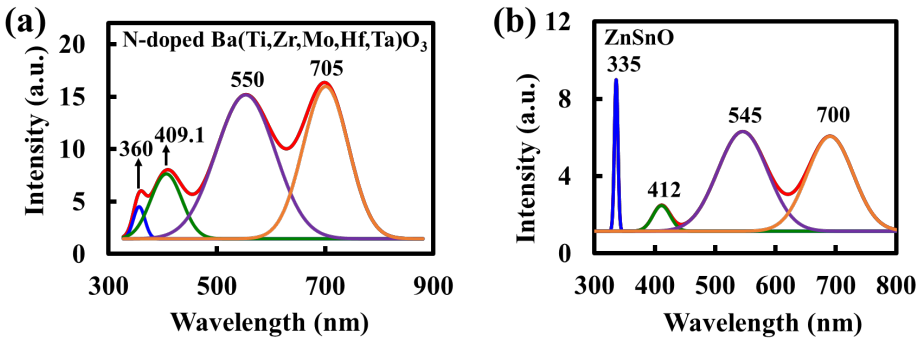


Figure S4. PL spectra of (a) N-doped Ba(Ti,Zr,Mo,Hf,Ta)O_3 and (b) ZnSnO.

Figure S5

Figure S5 compares the dielectric properties of the MIM structure before and after FGA treatment. Without FGA, low C_{ox} values are observed from 20 Hz to 1 MHz, and C_{ox} at 1 MHz is substantially lower than that at other frequencies (**Figure S5a**). However, when the configuration was treated with FGA at 350 °C for 40 min, there is only marginal frequency-dependent dispersion from 20 Hz to 1 MHz and substantially enhanced C_{ox} (**Figure S5b**), and both features reveal the effective minimization of existing D_{it} in the film. In the J_L–V characteristics of **Figure S5c** (inset: the measurement setup), the J_L value after FGA (blue color) is remarkably smaller than that before FGA (red color). Moreover, the J_L value after FGA (≈4.3 × 10^{-11} A·cm^{-2} at 1 V) is three orders of magnitude lower than that exhibited by other high-entropy-oxide-based devices reported in the literature [30, 34, 35].

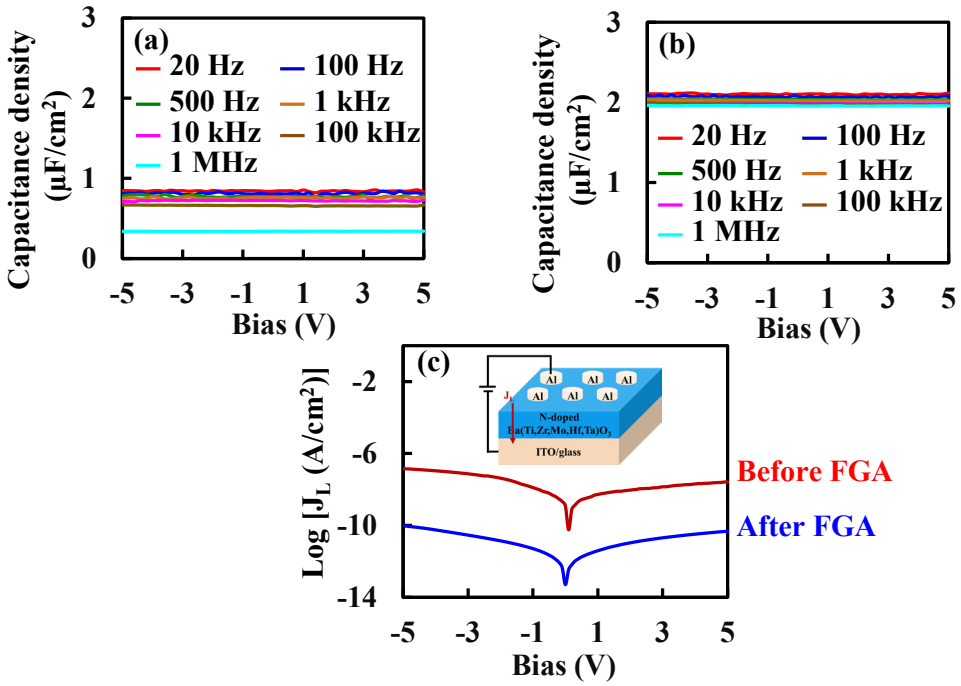


Figure S5. Dielectric properties for an MIM stack comprising favorable N-doped Ba(Ti,Zr,Mo,Hf,Ta)O_3. C–V curves from 20 Hz to 1 MHz (a) before and (b) after FGA. (c) J_L–V curves before (red) and after (blue) FGA.

Figure S6

To investigate the impact of each element in the N-doped $Ba(Ti,Zr,Mo,Hf,Ta)O_3$ film on the dielectric properties, N-doped medium-entropy-oxide [MEO, 3–4 elements on the B site, including $Ba(Ti,Zr,Hf)O_3$, $Ba(Ti,Hf,Ta)O_3$, $Ba(Ti,Zr,Ta)O_3$, and $Ba(Ti,Zr,Hf,Ta)O_3$] and N-doped low-entropy-oxide [LEO, 1–2 elements on the B site, including $Ba(Ti,Ta)O_3$, $Ba(Ti,Zr)O_3$, $Ba(Ti,Hf)O_3$, and $BaTiO_3$] films were studied (**Figure S6**). Their capacitance densities at 1 kHz (**Figure S6a)** and leakage current densities (**Figure S6b)** were improved when more principal elements were incorporated because of enhanced configurational entropy. N-doped $BaTiO_3$ exhibited the lowest capacitance densities ($k \approx 31$) and highest leakage current densities. By contrast, N-doped $Ba(Ti,Zr,Mo,Hf,Ta)O_3$ exhibited the most promising dielectric properties among them. To investigate the N-doping impact on the dielectric properties of $Ba(Ti,Zr,Mo,Hf,Ta)O_3$, the samples fabricated using various amounts of N_2 (0–4 sccm) with the same thickness were studied. These samples are named as N0, N1, N2, N3, and N4, respectively. From the C–V characteristics (**Figure S6c**), the enhanced capacitance density is observed with an increase in the amount of N_2 to 3 sccm. However, the value slightly decreases at N_2 = 4 sccm. The similar variation in the leakage current density is also observed (**Figure S6d**). The sample fabricated without any N_2 (N0) exhibited the lowest capacitance density and highest leakage current density. Their k values are displayed in **Figure S6e**. $Ba(Ti,Zr,Mo,Hf,Ta)O_3$ with $k \approx 147$ is observed. The N3 sample exhibited the most promising dielectric properties among the samples.

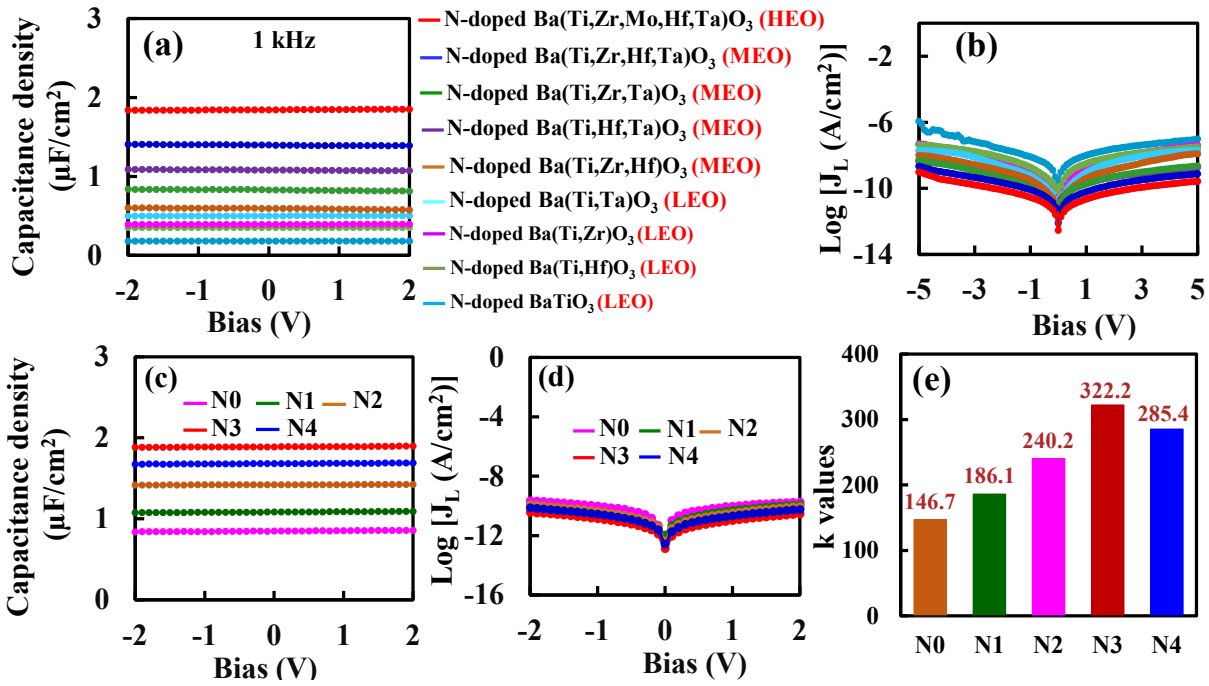


Figure S6. Dielectric properties exhibited by various HEO-, MEO-, and LEO-based MIM structures: (a) C–V curve (capacitance density measured 1 kHz) and (b) Log J_L–V curve. Dielectric properties exhibited by various N-doped Ba(Ti,Zr,Mo,Hf,Ta)O_3-based MIM structures at various amounts of N_2: (c) C–V curve (1 kHz), (d) Log J_L–V curve, and (e) associated *k* values.

Figure S7

The current on/off ratio and SS of all transfer characteristics for the device at various PGBS times without and with UV illumination are depicted in **Figure S7a** and **S7b**, respectively. Only minor changes are observed.

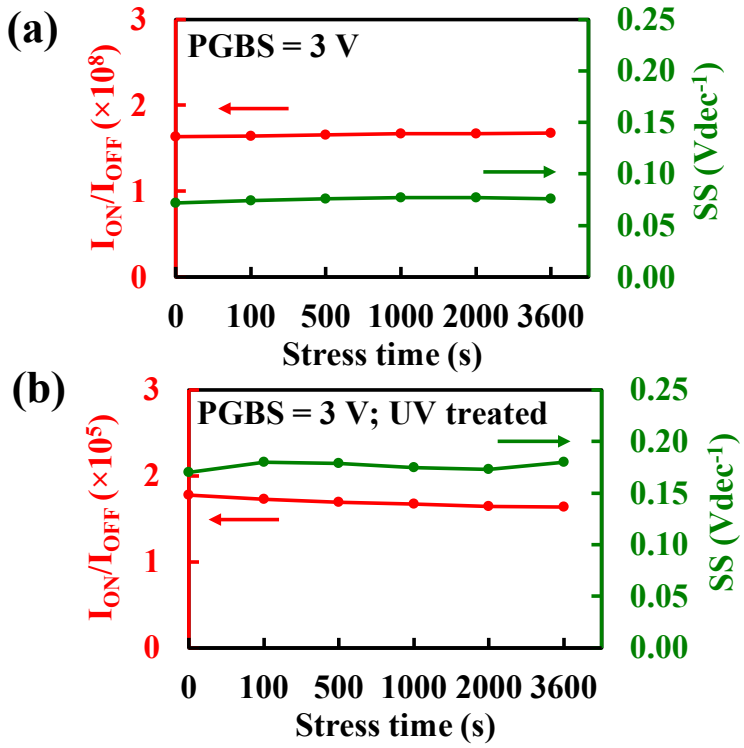
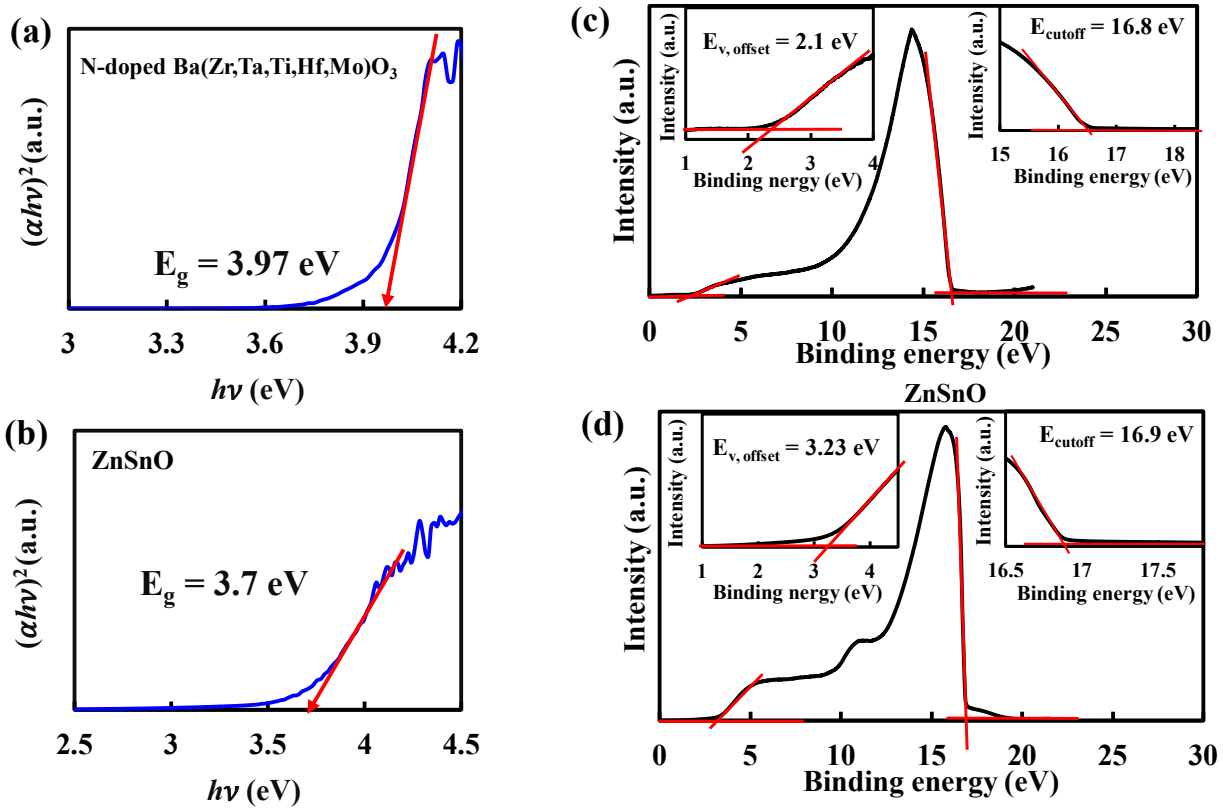


Figure S7. Current on/off ratio and SS variation at various PGBS times (a) without and (b) with UV illumination.

Figure S8

The energy band diagrams of the N-doped Ba(Ti,Zr,Mo,Hf,Ta)O_3 and ZnSnO layers in the TFT without any stress were constructed (**Figure S8**). UV–Vis spectroscopy was employed to obtain their E_g values (≈3.97 eV in **Figure S8a** and ≈3.7 eV in **Figure S8b**, respectively) through Tauc plots [$(\alpha h\nu)^2$ against $h\nu$, where α is the absorption coefficient, h denotes Planck's constant, and ν indicates the frequency]. The Φ values (≈4.4 eV in **Figure S8c** and ≈4.3 eV in **Figure S8d**, respectively) are obtained through UPS by subtracting the cutoff energy (E_{cutoff}) of the two films (upper right insets of **Figure S8c** and **S8d**, respectively) from the source energy (≈21.2 eV). The E_{Vmax} values of N-doped Ba(Ti,Zr,Mo,Hf,Ta)O_3 and ZnSnO (≈6.5 and 7.53 eV, respectively) were then calculated through the relationship of $E_{Vmax} = \Phi_S + E_{V,\,offset}$ (valence band offset), assuming $E_{V,\,offset}$ ≈ 2.1 eV for N-doped Ba(Ti,Zr,Mo,Hf,Ta)O_3 and 3.23 eV for ZnSnO, as indicated in the upper left insets of **Figure S8c** and **S8d**, respectively. The E_C values of ≈2.53 eV for N-doped Ba(Ti,Zr,Mo,Hf,Ta)O_3 and ≈3.83 eV for ZnSnO were then obtained through the equation of $E_C = E_{Vmax} - E_g$. The resulting energy band diagrams of the two films before and after contact on a vacuum scale are displayed in the left and right sides of **Figure S8e**, respectively. The diagram after contact helps elucidate the charge transport and trapping and photodetection behavior of the device, as discussed in **Figure 9** and **12**, respectively.



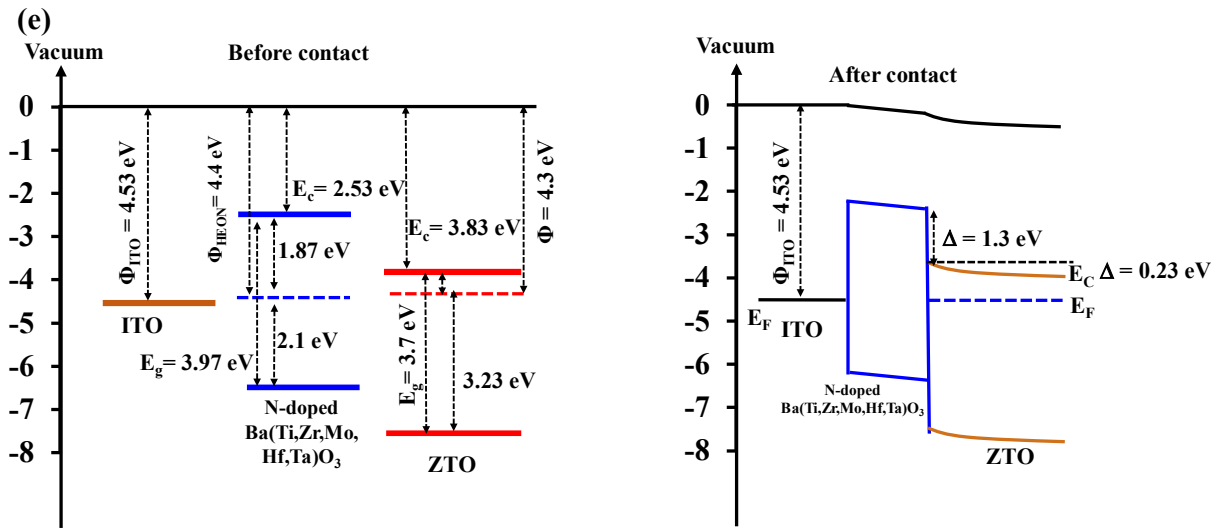


Figure S8. Tauc plots of (a) N-doped Ba(Ti,Zr,Mo,Hf,Ta)O_3 and (b) ZnSnO. UPS results of (c) N-doped Ba(Ti,Zr,Mo,Hf,Ta)O_3 and (d) ZnSnO. The upper right and upper left insets show the E_{cutoff} and $E_{V,\ offset}$ of the two films, respectively. (e) Energy band diagrams of the two films before (left) and after (right) contact.

Figure S9

The measurement procedure for NGBSI is illustrated in the lower right inset of **Figure S9a**, which is similar to that for PGBSI except for the application of NGBS = –3 V. In general, all transfer characteristics at various NGBS times (0–3600 s) without UV illumination (**Figure S9a**) also exhibit trivial variations in the current on/off ratio and SS (**Figure S10a**) and negligible changes in $I_{DS,\,max}$, which is further elucidated in the upper left inset (blue curve). These features indicate that no operation adjustment is needed for turning the device on and off, and there is no deterioration in the current flow. These curves also exhibit remarkable stability with only a small negative V_T shift ($\Delta V_T \approx -0.058$ V, orange curve in the upper left inset of **Figure S9a**) when the NGBS time increases from 0 to 3600 s. The associated energy band diagram is depicted in **Figure S9b**. Upward band bending of ZnSnO at the N-doped Ba(Ti,Zr,Mo,Hf,Ta)O_3/ZnSnO interface facilitates the trapping of holes induced by the negative electric field by neutral V_O-related traps (donor-like defects) in the E_g of N-doped Ba(Ti,Zr,Mo,Hf,Ta)O_3. When the NGBS time increases, more holes are induced, trapped, and distributed in the deep levels of the gap or into the bulk N-doped Ba(Ti,Zr,Mo,Hf,Ta)O_3. These accumulated hole traps induce a mirror layer of electrons (high charge carrier concentrations) in the ZnSnO channel layer, leading to a minor decrease in V_T ($\Delta V_T \approx -0.058$ V) [67-69]. However, when the device is additionally subjected to UV illumination (**Figure S9c**), all transfer curves at various NGBS times (0–3600 s) exhibit noticeable changes in the current on/off ratio and SS (**Figure S10b**). A remarkable increase in $I_{DS,\,max}$ (blue curve in the inset of **Figure S9c**) is also observed. Moreover, relative to the curve without UV illumination (black curve in **Figure S9c**), all curves under UV illumination are shifted substantially to negative V_{GS} ($\Delta V_T \approx -1.34$ V, orange curve in the inset of **Figure S9c**), indicating a high concentration of induced charge carriers in the channel because of the generation of electron–hole pairs by the light absorption of ZnSnO. The associated energy band diagram is depicted in **Figure S9d**, illustrating the generation of extra illumination-induced charge carriers and hole trapping (inducing mirror layers of electrons). Donor-like defects (*i.e.*, neutral V_O) are evident in the XPS (**Figure S3**) and PL (**Figure S4**) spectra.

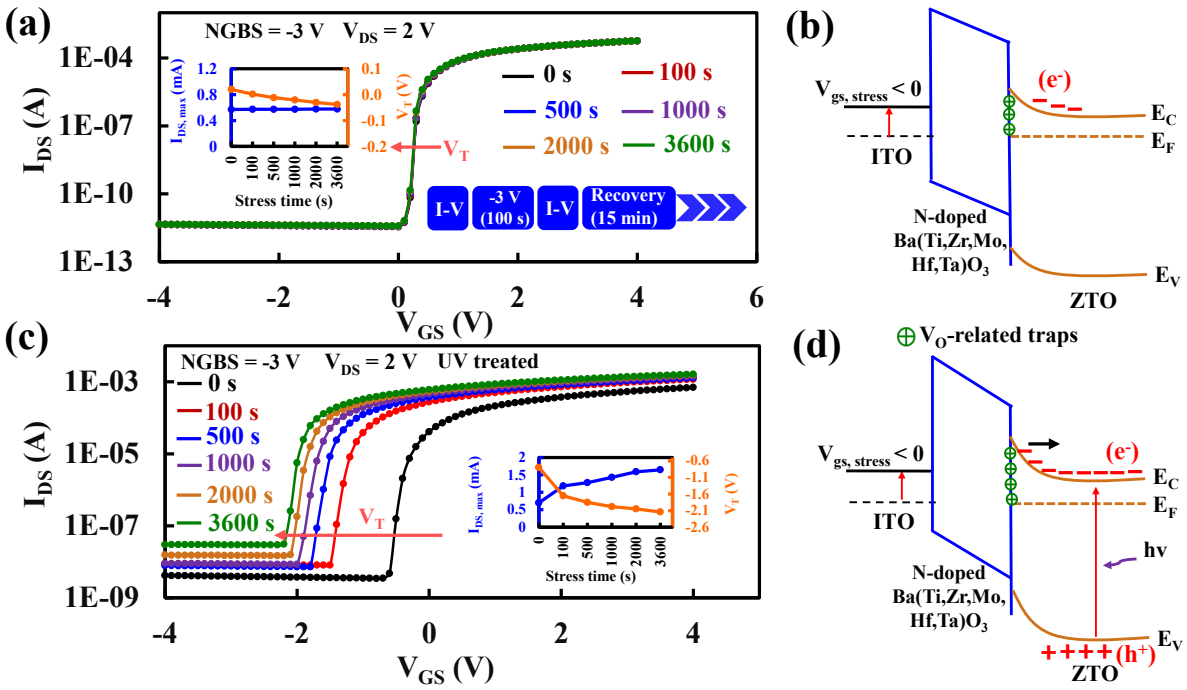


Figure S9. NGBSI study of the TFT at NGBS = –3 V for various times and V_{DS} = 2 V. (a) Transfer curves without UV illumination. The lower right and upper left insets show the measurement procedure and detailed variations in $I_{DS,\,max}$ and V_T, respectively. (b) Energy band diagram without UV illumination. (c) Transfer curves with UV illumination. The inset shows the detailed variations in $I_{DS,\,max}$ and V_T. (d) Energy band diagram with UV illumination.

Figure S10

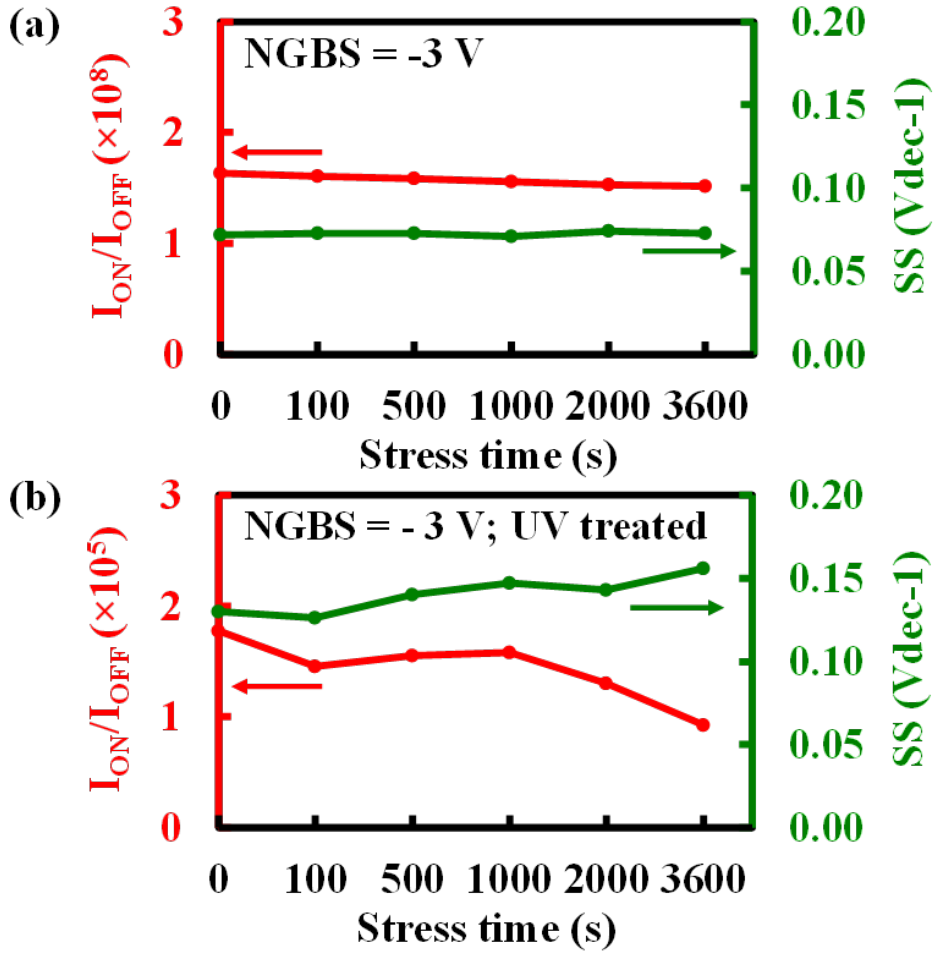


Figure S10. Current on/off ratio and SS variation of all transfer characteristics of the TFT at NGBS = –3 V for various times and V_{DS} = 2 V (a) without and (b) with UV illumination.

Figure S11

E_A measures the energy required for electrons to jump from E_F to E_C ($E_C - E_F$) in a thermal process, and a higher E_A indicates more difficulty for electron hopping. In the subthreshold region of transfer characteristics for a TFT, I_{DS} is described by Equation S1:[70]

$$I_{DS} = I_{D0} \times \exp[-E_A(V_{GS})/KT] \approx \alpha \times (V_{GS} - V_T) \times \exp[-E_A(V_{GS})/KT] \quad (S1),$$

where I_{D0} is a prefactor, $E_A(V_{GS})$ is the activation energy as a function of V_{GS}, K is the Boltzmann constant, and T is the temperature. Taking the logarithm on both sides of Equation S1, we obtain Equation S2.

$$\ln(I_{DS}) = [-E_A(V_{GS})/KT] + \ln \alpha \times (V_{GS} - V_T) \quad (S2).$$

Using Equation S2, $E_A(V_{GS})$ can be deduced from the plot of $\ln(I_{DS})$ against 1/KT.

Figure S11a and **b** plot the results for the device treated with NGBS (–3 V for 3600 s) and both NGBS and UV illumination from room temperature to 180 °C, respectively. The NGBS effect is elucidated by the observation of $E_A \approx 0.39$ eV ($V_{GS} = 0.2$ V) and a smaller slope (0.91 $eV \cdot V^{-1}$ (inset of **Figure S11a**) compared with that (0.94 $eV \cdot V^{-1}$) without any treatment (inset of **Figure 11a**). When the device was subjected to both NGBS and illumination, their respective impact on the induction of traps and carriers (accumulated holes inducing a mirror layer of electrons in ZnSnO) in the channel is reflected by a substantially smaller slope of 0.564 $eV \cdot V^{-1}$ and the considerably negatively shifted curve in V_{GS} with slightly reduced $E_A \approx 0.26$ eV (V_{GS} = –2.2 V, inset of **Figure S11b**).

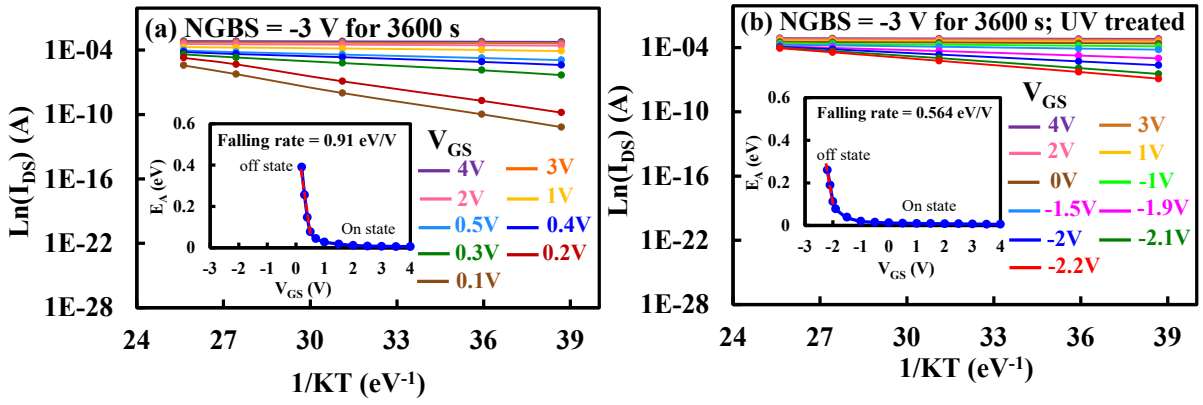


Figure S11. Plots of $\ln(I_{DS})$ against 1/KT (room temperature to 180 °C) at various V_{GS}, and $E_A(V_{GS})$ against V_{GS} (insets) of the TFT: (a) with NGBS (–3 V for 3600 s) and without UV illumination, and (b) with NGBS (–3 V for 3600 s) and UV illumination.